Climate Parameters from Satellite Spectral Measurements. Part I: Collocated AVHRR and HIRS/2 Observations of Spectral Greenhouse Parameter

RICHARD A. FREY AND S. A. ACKERMAN

Cooperative Institute for Meteorological Satellite Studies, University of Wisconsin-Madison, Madison, Wisconsin

BRIAN J. SODEN

Atmospheric and Oceanic Sciences Program, Princeton University, Princeton, New Jersey

ABSTRACT

An automated method of monitoring various climate parameters using collocated Advanced Very High Resolution Radiometer (AVHRR) and High-Resolution Infrared Sounder-2 (HIRS/2) observations has been developed. The method, referred to as CHAPS (collocated HIRS/2 and AVHRR products) was implemented during the months of July 1993 and January and July 1994. This paper presents the oceanic cloud screening method and analysis of the spectral greenhouse parameter (g_λ) for July 1993 and January 1994. In addition, the CHAPS derived clear-sky parameters are compared to the NESDIS historical dataset. There is agreement between NESDIS and CHAPS for the $g_{6.7}$ and $g_{7.3}$. The NESDIS 8.2-μm data appears to be cloud contaminated. Through comparison with CHAPS, it is suggested that the mode, rather than the mean, provides the better estimate of the central tendency of the NESDIS clear-sky 8.2-μm radiance distribution, particularly for regions with extensive low-level cloud cover.

It is shown that the spectral greenhouse parameter at wavelengths sensitive to middle and upper atmospheric water vapor content is dependent on SST via its connection to large-scale atmospheric circulation patterns. It is also shown that the variability of the spectral greenhouse parameter is strongly a function of latitude at these wavelengths, as well as in spectral regions sensitive to lower-level water vapor. Standard deviations are largest in the Tropics and generally decrease poleward. In contrast, variability in the spectral regions sensitive to upper-tropospheric temperature peaks in the middle latitudes and has its minimum in tropical latitudes.

Variability in the relationship between g_λ and SST shows only a weak dependence on season for channels sensitive to water vapor content. A strong seasonal dependence is found in the $g_{14.2}$ for the middle-latitude regions associated with changes in the temperature structure of the upper troposphere.

The relationship between the spectral greenhouse parameter and the broadband greenhouse parameter is presented and discussed. It is found that the range in broadband g for warm tropical SSTs is driven by spectral changes at wavelengths sensitive to upper-tropospheric water vapor. For cooler SSTs associated with the middle latitudes, the range in g is a function of the spectral greenhouse parameter sensitive to the temperature structure of the upper troposphere.

1. Introduction

The satellite platform provides a means for global monitoring of various earth-system parameters. Long-term satellite datasets spanning time periods of up to 20 years are now becoming available for use in the investigation of climate trends and variability. Although such time intervals are usually considered too short for climate studies, any effort to systematically analyze a time series of global satellite data of even that length would be extraordinarily costly. To avoid

the expense of retrieving data from archives, the authors have developed a method whereby observations from two instruments on the same space platform are combined in a near real-time environment. Various climate parameters are computed and analyzed in the same time frame. Similar algorithms could conceivably be expanded to include more instruments and be operated over long time periods in order to automatically monitor important atmospheric variables such as cloud type and amount, cloud radiative forcing, and the "greenhouse effect" of the atmosphere.

This paper is the first in a series of investigations of various climate parameters using global satellite spectral observations. These global measurements are used to study interannual and interseasonal variations. The global data also provide validation for climate models and will lead to interesting insights on atmospheric pro-

Corresponding author address: Dr. Richard A. Frey, Cooperative Institute for Meteorological Satellite Studies, University of Wisconsin-Madison, 1225 West Dayton Street, Madison, WI 53706. E-mail: raf@ssec.wisc.edu

TABLE 1. HIRS/2 channel spectral responses and descriptions (after Kidwell 1991).

Channel #	Central wavenumber (cm⁻¹)	Central wavelength (microns)	Appx. peak in wt. function (mb)	Description
1	667.58	15.0	30	15 micron
2	680.18	14.7	60	CO_2 band
3	690.01	14.5	100	CO_2 band
4*	704.22	14.2	250	CO_2 band
5*	716.32	14.0	500	CO_2 band
6*	732.81	13.7	750	CO_2 band
7*	751.92	13.3	900	CO_2 band
8*	900.45	11.1	surface	window
9	1026.66	9.7	25	ozone
10*	1223.44	8.2	900	water
11	1368.68	7.3	600	vapor
12	1478.59	6.7	400	vapor
13	2190.37	4.6	950	4.3 micron
14	2210.51	4.52	850	CO_2 band
15	2236.62	4.47	700	CO_2 band
16	2267.22	4.1	600	CO_2 band
17	2361.44	4.2	5	CO_2 band
18	2514.68	4.0	surface	CO_2 band
19	2653.48	3.8	surface	window
20	14 500.00	0.69	—	visible

* Indicates a channel used in CHAPS cloud clearing.

cesses relevant to climate change studies. Part I focuses on the methods of data collection and clear-sky determination, along with analysis of the spectral greenhouse parameter. Variations in clear-sky observations from various spectral bands across the infrared spectrum are investigated, as well as their relation to the broadband observations.

The algorithm designed to operate in near real time for the purpose of monitoring climate parameters and which makes use of collocated radiance measurements from the Advanced Very High Resolution Radiometer (AVHRR) and the High Resolution Infrared Sounder/ 2 (HIRS/2) is referred to as CHAPS (collocated HIRS/2 and AVHRR Products). Observations from instruments aboard the *NOAA-12* space platform were used in conjunction with forecast model output from the National Meteorological Center (NMC) to produce global distributions of cloud altitude and amount, the spectral greenhouse effect of the atmosphere, and spectral cloud radiative forcing. This study utilizes CHAPS data collected during the months of July 1993 and January 1994 for the purpose of studying the spectral properties of the clear-sky atmosphere.

The feasibility of collocating measurements from two instruments and analyzing the combined data in near real time is also demonstrated. The technique discussed below can, therefore, be adapted into an operational algorithm but could be applied to historical datasets as well. In this paper, the emphasis on collocating AVHRR pixels within the HIRS/2 footprints is to ensure cloud-free HIRS/2 scenes. A complete discussion of the spectral measurements and the CHAPS cloud-screening process for ocean surfaces is found in

section 2. Comparison of the CHAPS-derived clear-sky parameters with those derived from the historical National Environmental Satellite Data and Information Service (NESDIS) operational radiances is given in section 3. Analysis of the spectral greenhouse parameter is undertaken in section 4, and the results of the study are summarized in section 5.

2. Satellite observations

Adequate discrimination between clear and cloudy scenes from space is crucial for an understanding of global radiation balance, cloud cover, surface property studies, and retrieval of atmospheric temperature and moisture profiles. The description and understanding of the earth's clear regions is important for its own sake, but also as a reference for changes in radiative forcings caused by differing cloud types and amounts. By combining the spectral resolution of an atmospheric sounder (HIRS/2) with the spatial resolution of an imager (AVHRR), we hope to more accurately describe the radiative properties of clear-sky regions. Hayden and Taylor (1985) and Levanant (1989) used collocated AVHRR and HIRS/2 observations to improve clear-sky HIRS/2 scenes and thus improve the atmospheric profiling of the TOVS package. Ackerman et al. (1992) used collocated AVHRR, HIRS/2, and ERBE observations to study clear- and cloudy-sky radiative properties. Collocated AVHRR and HIRS/2 data have also been used to study cloud properties (e.g., Baum et al. 1992, 1994). Derrien et al. (1993) make use of the AVHRR to assess the cloud conditions within the HIRS/2 footprint and have developed

an automatic regional cloud detection technique for the *NOAA-11* using AVHRR 1-km data. In this paper we present an automated global cloud detection technique using the AVHRR and HIRS/2 data in tandem.

Tables 1 and 2 list channel information for the HIRS/2 and AVHRR instruments aboard *NOAA-12*. The spatial resolution of the HIRS/2 is nominally 17 km at nadir, while that of the AVHRR is 1 km. The present study utilized AVHRR global area coverage (GAC) data, where every third scanline was recorded and four of each five-pixel group along these scanlines were averaged, resulting in a nominal resolution of 4 km. The *NOAA-12* space platform is in near-terminator sun-synchronous orbit with an inclination of approximately 110 deg and height of 850 km. Such an orbit provides near-global coverage in 24 h, with observations near 0730 and 1930 local time for most latitudes. This allows monitoring of day to day changes in clear-sky radiative properties due to variations in atmospheric moisture and temperature. This is particularly important in areas of the world that are otherwise very data sparse. Using the methodology described below, it is possible to build an archive of high-quality clear-sky parameters over the world's oceans. Such a dataset now exists for the months of July 1993 and January and July 1994.

a. Data acquisition and processing

The radiance data were acquired in near real time from the Man-computer Interactive Data Access System (McIDAS) at the University of Wisconsin—Madison (Suomi et al. 1983). Calibrated and navigated AVHRR and HIRS/2 measurements (Kidwell 1991) are stored on an IBM 4381 mainframe several hours after the completion of each orbit by the spacecraft. These datasets remain on the computer for approximately 24 h, until being overwritten by more recent observations. Global fields of vertical temperature and moisture profiles were obtained from the NMC in Camp Springs, Maryland. These "final analysis" fields are output for 000 and 1200 UTC and are available approximately 10 h later. Weekly, global Reynolds' blended sea surface temperatures (SSTs) were also received from the NMC.

Because of the tremendous volume of data, particularly from the AVHRR, processing had to be completed in a timely fashion to reduce the amount and cost of storage space. This was accomplished with the use of an IBM RISC 6000 computer. When new orbital data appeared on the mainframe, it was transferred to the RISC 6000 by use of the standard File Transfer Protocol (ftp) software. A preprocessing program was run periodically to ascertain which ancillary datasets would be needed (e.g., NMC profiles that would not be available for several hours) to match up the HIRS/2 and AVHRR orbital datasets, and to generate any other parameters necessary for processing. The input

NMC temperature and moisture fields were linearly time interpolated, when necessary, to the nearest hour of the orbital start times. Such a scheme is adequate for processing over the ocean surface where diurnal temperature variations are very small. This software acted as a funnel, gathering data from several machines, usually at several different times, providing the main processing stream with all of the information needed to process one complete orbit.

The central and most computation-intensive task of the data processor is the collocation of the AVHRR GAC pixels within the larger HIRS/2 footprints. The method described by Aoki (1980) was chosen, but where GAC data is used in place of the 1-km local area coverage (LAC) type. This method has been used with good success by the present authors (Ackerman et al. 1992). Although the attempt was made to process as much data as possible, in order to minimize problems associated with limb measurements, sun glint, and angular effects on visible measurements, fields of view (FOVs) beyond 30 deg of nadir were eliminated from the collocation. Also, poleward of 70° latitude only one of four HIRS/2 FOVs was collocated with AVHRR pixels, due to the oversampling by polar orbiters in these regions. By restricting scan width, the amount of time needed to achieve truly global coverage is lengthened to two days, but any given geographical area is observed at least once for four consecutive days near the equator and more often nearer the poles. Even with the above restrictions, approximately 20 000 collocated HIRS/AVHRR FOVs were produced per orbit with about 30 AVHRR GAC observations for each HIRS/2. The collocated measurements (as well as all derived products) were mapped onto a 2.5° lat equal-surface-area grid according to the International Satellite Cloud Climatology Project (ISCCP) binning scheme (Rossow and Schiffer 1991).

A check on the quality of the collocations is readily accomplished by comparison of the 11-μm "window" channel measurements of each instrument. Given that the atmosphere is nearly transparent at this wavelength, both instruments sense a wide variety of scene temperatures as the spacecraft progresses in its orbit. AVHRR pixel radiances were averaged over the corresponding HIRS/2 FOVs and converted to equivalent temperatures, then compared to those of the single HIRS/2 measurements. AVHRR data were also corrected for the known nonlinearity of calibration in the three infrared channels (Brown 1991). Correlations over an orbit were generally greater than 0.99. Because it is convenient in terms of computer processing efficiency, three other algorithms are executed during the collocation step. First is the CO_2-slicing method of cloud altitude determination (Smith et al. 1974; Smith and Platt 1978; Menzel et al. 1983) using five of the HIRS/2 infrared channels. This information is used as part of a quality control system for clear-sky determination later in the processing stream. Secondly, histograms of

TABLE 2. AVHRR channel spectral responses and descriptions (after Kidwell 1991).

Channel	Central wavenumber (cm^{-1})	Central wavelength (microns)	Approximate peak in weight function (mb)	Description
1	15 673.98	0.64	—	visible
2[a]	11 997.60	0.83	—	near-IR
3[a]	2639.61	3.8	surface	window
4[a]	921.03	10.9	surface	window
5[a]	837.36	11.9	surface	water vapor continuum

[a] Indicates a channel used in CHAPS cloud clearing.

AVHRR pixel values for each of its five channels are produced for each ISCCP region viewed. The class widths are 0.5 K for infrared channels and 1% for the visible. Only those pixels found to be located within HIRS/2 FOVs are incorporated into the histograms, which saves considerable amounts of computer time. Figure 1a shows a typical subtropical regional histogram of AVHRR 11-μm brightness temperatures. Figure 1b is similar but incorporates only the collocated pixels that fall inside HIRS/2 footprints. It is clear that the second histogram captures the important thermal
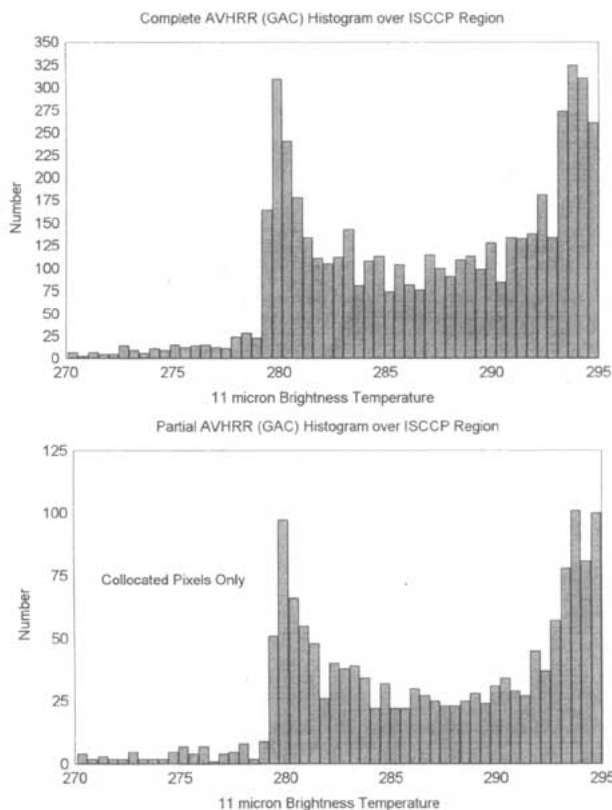

FIG. 1. (a) Histogram of AVHRR (GAC) 11-μm brightness temperatures from an entire ISCCP region centered at 26.3°N and 90.7°W. (b) Histogram of AVHRR (GAC) 11-μm brightness temperatures taken from collocated HIRS/2 footprints. Region is centered at 26.3°N and 90.7°W.

characteristics of the region. Third, an estimate of total precipitable water at the location of each HIRS/2 FOV is computed based on spatially and temporally interpolated NMC temperature and moisture profiles.

b. Clear-sky determination

Using HIRS/2 spectral measurements and AVHRR GAC collocated pixel data, an attempt is made to determine which HIRS/2 FOV locations (if any) are clear within each ISCCP region viewed. Information from any such FOVs are used to infer the regional mean clear-sky radiative characteristics.

An important part of this process is the generation of regional 11-μm clear-sky brightness temperature threshholds. The first step is to compute a first guess clear-sky brightness temperature threshhold at each HIRS/2 FOV location in the region.

Based on total precipitable water (TPW) estimates noted above, HIRS/2 scan angles (SCNA), and collocated AVHRR radiance data from a wide variety of ocean scenes, the following regression equation was developed:

$$\text{SFCDIF} = A0 + \left[\frac{A1 \times \text{TPW}}{\cos(\text{SCNA})} \right]$$

$$+ \left\{ A2 \times \left[\frac{\text{TPW}}{\cos(\text{SCNA})} \right]^2 \right\}, \quad (1)$$

where SFCDIF is the difference between the Reynolds' blended SST and the mean collocated AVHRR brightness temperature at a given FOV location. The values of the coefficients are $A0 = -0.8163$, $A1 = 0.5488$, and $A2 = 0.1132$.

The first guess threshhold (FGT) may then be written,

$$\text{FGT} = \text{SST} - \text{SFCDIF} - 4.0. \quad (2)$$

The extra four degrees subtracted from the SST is to account for the standard lapse rate from the surface to the minimum expected cloud base.

Making use of the computed variabilities of collocated AVHRR pixels and the FGT associated with each HIRS/2 FOV location in a region, individual GAC 11-μm measurements within each HIRS/2 FOV are sorted

Regional AVHRR (GAC) Histogram
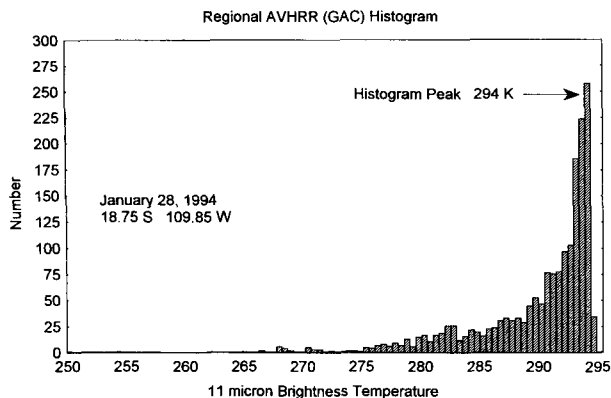
FIG. 2. Regional histogram of AVHRR 11-μm
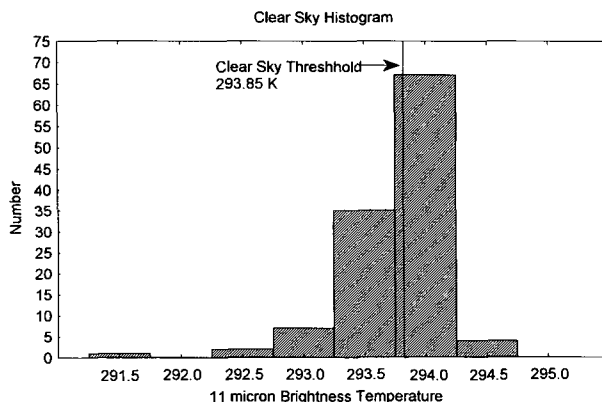brightness temperatures.

Clear Sky Histogram

FIG. 3. Histogram of AVHRR 11-μm observations, which met
the "possibly clear-sky" criteria (see text).

into *possibly clear* and *possibly cloudy* categories. During nighttime situations (solar zenith angles greater than or equal to 80 deg), if the standard deviation of 11-μm collocated observations is less than or equal to 0.5 K, then each 11-μm pixel value is compared with the FGT for that HIRS/2 FOV location. Measurements with brightness temperatures greater than or equal to the FGT are incorporated into a second, (possibly) clear-sky histogram (CSH). During daytime situations (solar zenith angle less than 80 deg), the further requirement is made that the AVHRR channel 2 reflectance be less than or equal to a threshold (e.g., 6.5%). This process is repeated for all HIRS/2 FOV locations in the ISCCP region. The final clear-sky 11-μm brightness temperature threshhold is defined as the temperature corresponding to the class of maximum frequency in the CSH minus the standard deviation computed from all of the *possibly clear* pixel values. It should be noted here that single-pixel measurements at 3.7 μm (channel 3), which could be useful in cloud screening, are not used in the algorithm due to the known low signal-to-noise characteristics of this channel.

The FGT and AVHRR FOV variability are used together to minimize cloud contamination. The variability check screens out collocated FOVs, which may contain warm AVHRR measurements, but have a high probability of being cloud contaminated. It also flags FOVs containing thin cirrus clouds, which are often characterized by warm brightness temperatures and low visible reflectance measurements. By use of Eq. (2), we attempt to define a brightness temperature that includes pixels from reasonably warm scenes, but excludes those colder, cloudy areas that may be very uniform. The daytime channel 2 reflectance test is an additional check for warm clouds such as stratus or fog, which are bright in the visible wavelengths. When all of the AVHRR 11-μm measurements from pixels that passed the *possibly clear* tests are sorted into the CSH, observations from clear scenes will cluster into a sharp, narrow peak characteristic of the desired clear-sky

brightness temperature. Those from partly cloudy areas form a broader, ill-defined peak with fewer observations because of the higher temperature and moisture variability in those scenes. The standard deviation of the CSH AVHRR 11-μm values is subtracted from the peak temperature to allow for instrument noise in the measurements.

Figure 2 shows a histogram describing an ISCCP region centered on 18.75°S, 109.85°W on 28 January 1994. Figure 3 shows the associated CSH as well as the final clear-sky threshhold. A time series of clear-sky threshhold values, Reynolds' blended SSTs, and maximum collocated AVHRR 11-μm observed brightness temperatures is shown in Fig. 4 for the ISCCP gridbox centered on 18.75°S, 107.13°W. Time runs through the month of January. Note that very little or no data was archived for a few days due to poor data quality or data ingest problems. Data may also be missing for a given day due to large scan angles. The two low points found on days 11 and 25 occur because no
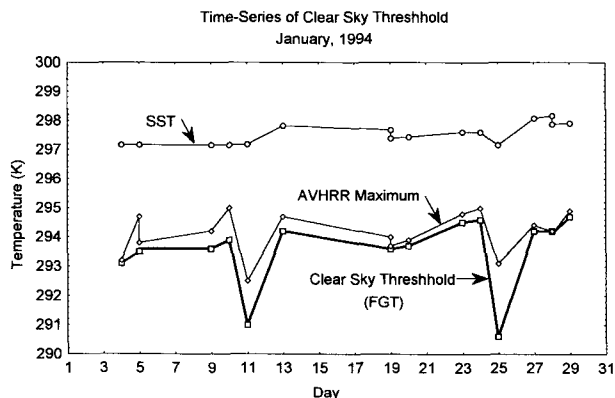
Time-Series of Clear Sky Threshhold
January, 1994

FIG. 4. Time series of Reynolds' blended SST, regional maxima of mean collocated AVHRR 11-μm observations and clear-sky threshholds for the month of January 1994. Region is centered at 18.75°S, 107.13°W.

FOVs satisfying the *possibly clear-sky* criteria were found. The threshhold represented in the figure is the first guess. On these two days there are no high-confidence clear footprints and thus no clear-sky spectral greenhouse parameter is derived. Note that the maximum AVHRR values are also low on these days, while the SST remains nearly constant.

Final clear-sky determination for each HIRS/2 FOV location is accomplished by use of the regional clear-sky threshhold along with several other criteria. If each of the criteria are met, the FOV in question is said to be clear. They are

- If daytime, mean collocated AVHRR channel 2 refectance less than or equal to 6.5.
- Mean collocated AVHRR 11-μm brightness temperature greater than or equal to the regional clear-sky threshhold.
- Collocated AVHRR 3.7-μm standard deviation less than or equal to 0.5 K.
- Collocated AVHRR 11-μm standard deviation less than or equal to 0.5 K.
- HIRS/2 8–11-μm brightness temperature difference less than −3.5 K.
- Mean collocated AVHRR 11–12-μm brightness temperature difference greater than 0.5 K.
- Computed cloud height from CO_2-slicing algorithm greater than 500 mb.

Tests 1, 2, and 4 have already been discussed, except that here we apply tests 1 and 2 to entire HIRS/ AVHRR FOVs instead of one GAC pixel. Test 3 is included as an additional test for the presence of low, warm clouds, being particularly effective in daylight hours.

The last three tests take advantage of the multiple spectral channels of both instruments. Due to spectral differences in atmospheric absorption of upwelling radiation due to cloud liquid water between 8 and 11 μm, versus that of ice, fully overcast FOVs containing ice cloud exhibit positive 8–11-μm differences, while those filled with water cloud show negative differences. The magnitude of the differences also depends on the total column water vapor amount. Therefore, given the same temperature and moisture conditions, clear-sky FOVs will yield greater negative differences than those contaminated with water cloud. At the same time, the presence of ice clouds (e.g., thin cirrus) also drives differences more positive. Strabala et al. (1994) use a threshhold value of 0.5° in defining clear-sky scenes observed with the MAS [MODIS (Moderate-Resolution Imaging Spectrometer) Airborne Simulator] instrument. The difference between the two threshholds is due to the wider bandwidths of the HIRS/2 8 and 11 μm channels.

On the other hand, 11–12-μm brightness temperature differences approach 0 with total water cloud coverage, but show small positive differences in clear-sky conditions, owing to differential water vapor absorp-

tion properties between the two wavelengths (Inoue 1987). This test is useful as another check for low clouds having very uniform temperatures.

The cloud height test is a final check for the presence of middle and high level clouds. The CO_2-slicing method is very reliable in detecting clouds of these types (Menzel et al. 1983; Smith and Platt 1978).

The clear-sky detection is summarized in two flow charts in Figs. 5 and 6. The first shows the steps in computing a regional clear-sky threshhold, the second details the final determination process for each FOV. These tests were incorporated into the CHAPS algorithm to optimize detection of clear-sky HIRS/2 observations. The algorithm and data structures were designed so that reprocessing of the data is a straightforward process.

3. Comparison with NESDIS operational radiances

This section compares climatologies of clear-sky radiances derived from the CHAPS procedure outlined above with HIRS/2 clear-sky radiances obtained from the TOVS operational sounding products dataset. The TOVS sounding product dataset contains clear-sky radiances from HIRS/2 as well as other TOVS instru-
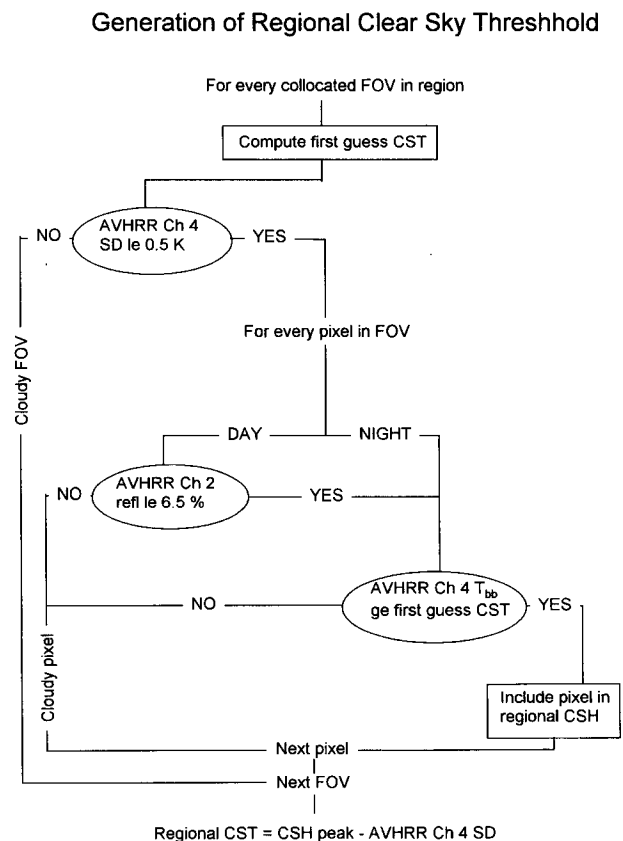
Generation of Regional Clear Sky Threshhold

For every collocated FOV in region

Compute first guess CST

NO ← AVHRR Ch 4 SD le 0.5 K → YES

Cloudy FOV

For every pixel in FOV

DAY ──── NIGHT

NO ← AVHRR Ch 2 refl le 6.5 % ── YES

Cloudy pixel

NO ──── AVHRR Ch 4 T_{bb} ge first guess CST ── YES

Include pixel in regional CSH

Next pixel

Next FOV

Regional CST = CSH peak - AVHRR Ch 4 SD

FIG. 5. Flowchart showing the steps in computing a regional clear-sky threshhold.
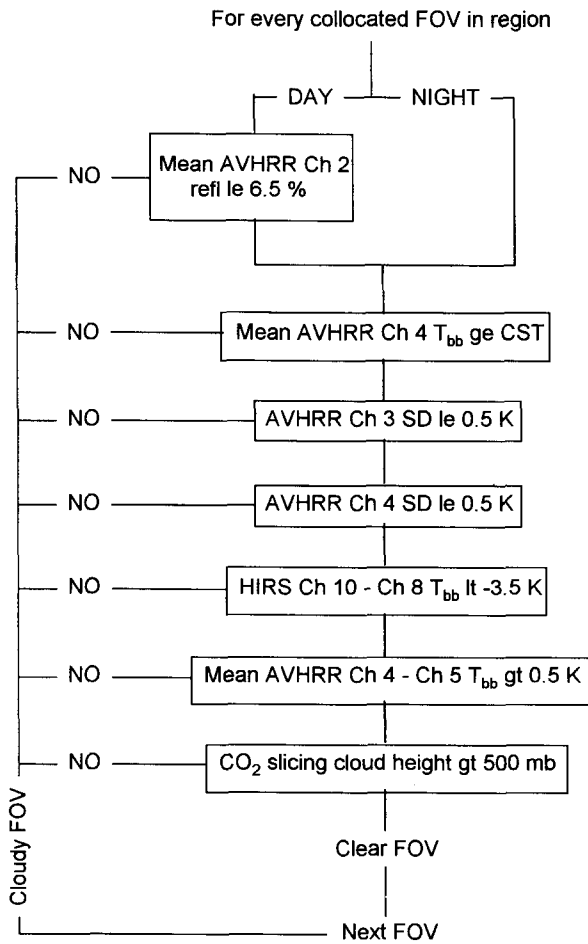
Final Clear Sky Determination

For every collocated FOV in region

FIG. 6. Flowchart showing the final clear-sky determination process for each collocated FOV.

are relevant to the comparison: 1) cloud clearance— the NESDIS operational cloud clearance algorithm, commonly referred to as the "N*" technique (Smith et al. 1979; McMillin and Dean 1982), applies thresholds to the HIRS/2 radiance field to discriminate between clear and cloudy pixels. The most significant difference between this approach and the CHAPS procedure is the latter's use of high spatial resolution AVHRR measurements to determine the horizontal homogeneity of the radiance field within the HIRS/2 FOV. This feature enables more reliable discrimination between clear and partially cloud-filled HIRS/2 observations and is particularly useful for identifying low-level clouds, which may not produce a strong enough IR signature to be detected by NESDIS thresholds. 2) Angular correction—in addition to cloud clearance, NESDIS performs a limb correction that converts the original HIRS/2 radiances viewed at varying zenith angles to equivalent "nadir-view" radiances. No limb correction is performed in the CHAPS processing, instead radiances are restricted to within 30 deg of nadir.

Following Ackerman et al. (1992), we define a normalized spectral greenhouse parameter as

$$g_\lambda = \frac{B(T_s) - I_{\lambda cs}}{B(T_s)}, \qquad (3)$$

where $B(T_s)$ is the Planck function at wavelength λ and surface temperature T_s, and $I_{\lambda cs}$ is the satellite observed clear-sky radiance. SSTs are derived from the collocated mean AVHRR clear-sky observations using the NOAA operational algorithm (McClain 1989; Wade 1993). Figure 7 shows the zonally averaged spectral greenhouse parameter from CHAPS (solid line) and NESDIS (dashed line) for January from three different spectral channels; 6.7 μm, 7.3 μm, and 8.2 μm. The CHAPS data are from January 1994, whereas the NES-

ments (MSU and SSU) used by NESDIS to produce operational retrievals of temperature and moisture, which are subsequently distributed for assimilation into numerical weather prediction models. The objectives of this comparison are 1) to demonstrate the consistency between the two clear-sky radiance climatologies and 2) highlight regions of discrepancy between the two radiance datasets, which are attributable to differences in the processing of the input radiance data stream. In particular, it will be shown that in certain climatological regions, the present cloud clearance algorithm provides significantly improved clear-sky radiance determination for atmospheric channels whose weighting functions peak in the lower atmosphere.

There are two important differences between the operational data processing performed by NESDIS and the CHAPS processing (described in section 2), which
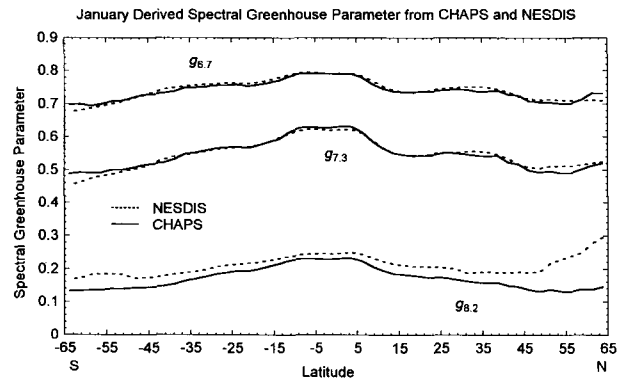

FIG. 7. Oceanic zonal mean spectral greenhouse parameter from CHAPS (solid lines) and NESDIS (dashed lines) at 6.7 μm (top), 7.3 μm, (middle) and 8.2 μm (bottom). CHAPS data are from January 1994, whereas that of NESDIS includes January data from 1981 to 1990.

DIS data represent a climatological average of Januarys from the period 1981–1990. The data represent zonal averages over ocean surfaces only. For channels whose weighting functions peak in the upper troposphere (6.7 μm, 7.3 μm), zonal variations in the greenhouse parameter are in good agreement with each other. Differences are typically less than 2%, or roughly 0.5 K in terms of equivalent brightness temperatures. The study of Bates and Wu (1995) suggests that intercalibration differences in 6.7-μm brightness temperatures between successive NOAA satellites is between 0.1 and 0.5 K.

Larger discrepancies between CHAPS and the NESDIS observations exist for the lower tropospheric water vapor sensitive channel (8.2 μm). In particular, for latitudes poleward of 40° the NESDIS data exhibit a significantly larger greenhouse parameter especially in the Northern (winter) Hemisphere where differences range from 50% to 100%. These differences reveal that the NESDIS radiances at 8.2 μm are systematically colder than the CHAPS radiances. A similar pattern of discrepancy is noted over the Southern Hemisphere midlatitudes during July (not shown).

A comparison of the two datasets as a function of SST is presented in Fig. 8. Individual points correspond to CHAPS radiances. The solid and dashed lines correspond to the mean and ±1 standard deviation of the NESDIS radiances binned as a function of SST. Good agreement is apparent for the upper-tropospheric channels (6.7 μm and 7.3 μm) illustrating that both climatologies show a nearly identical dependence upon SST. Both climatologies exhibit an increase in g_λ with increased SST and a nonlinear rise at the warmest SSTs; however, in the 8.2-μm channel, the NESDIS green-

house parameter is systematically larger than the CHAPS greenhouse parameter. The discrepancy is greatest for cold SSTs, consistent with the zonal average plots shown above. Indeed, for cold SSTs, the NESDIS data depict a slight decrease in g_λ with increasing SST. This is contrary to what is expected based upon observations that atmospheric water vapor generally increases with increasing SST (Stephens 1990). This comparison suggests that the NESDIS 8.2-μm radiances contain a systematic cold bias, particularly over cold, midlatitude ocean surfaces.

The presence of a cold bias in the NESDIS radiances for only the 8.2-μm channel suggests a contamination of the NESDIS clear-sky radiances by low cloud cover. This is consistent with the observation of largest bias over cold, midlatitude oceans where low cloud cover is most frequent. To examine this issue in more detail, Fig. 9 compares a histogram of the instantaneous (daily) NESDIS oceanic, clear-sky 8.2-μm brightness temperatures (BT) with results from CHAPS for two geographic regions: (top) Northern Hemisphere midlatitudes (45°–55°N) and (bottom) the subtropics (20°–30°N). A distinct skew in the histogram toward lower BT is apparent in the NESDIS values. This supports the hypothesis that the NESDIS radiances are cloud contaminated by low cloud cover. Since clouds are generally colder than the underlying atmosphere/surface, classification of partially cloudy FOVs as clear results in a tail of cloud contaminated BT extending toward lower values. The CHAPS BT (dark wide bars) on the other hand, exhibit a much more Gaussian distribution consistent with that expected for completely cloud-free FOVs. The maximum values in the two his-
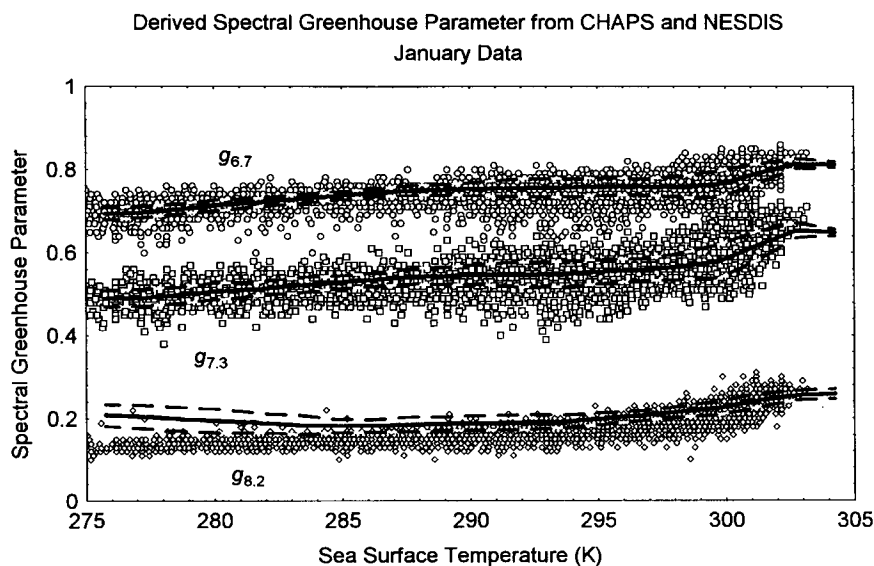
Derived Spectral Greenhouse Parameter from CHAPS and NESDIS

January Data

FIG. 8. Oceanic spectral greenhouse parameter from CHAPS (dots) and NESDIS (lines) at 6.7 μm (top), 7.3 μm (middle), and 8.2 μm (bottom) as a function of SST for January. Solid and dashed lines represent the mean and ±1 standard deviation of the NESDIS values.

HIRS Clear Sky 8.2 micron Brightness Temperatures
January
Ocean Surfaces from 45 to 55 North Latitude

HIRS Clear Sky 8.2 micron Brightness Temperatures
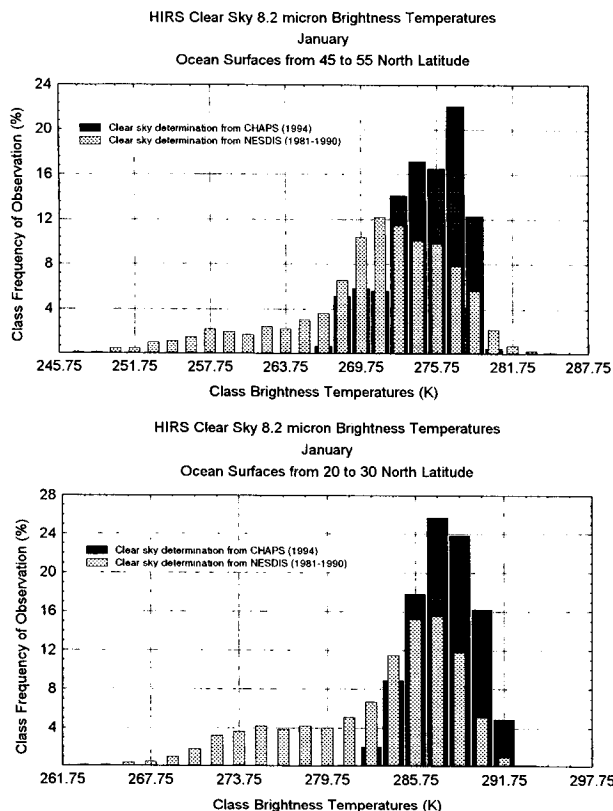January
Ocean Surfaces from 20 to 30 North Latitude

FIG. 9. Frequency histogram of observed HIRS/2 oceanic clear-sky 8.2-μm brightness temperatures from 45°–55°N latitude (top) and 20°–30°N (bottom). Dark wide bars indicate clear-sky determination using the CHAPS algorithm for January 1994. Lighter bars denote clear-sky determination using the NESDIS (TOVS) algorithm for January during 1981–1990.

tograms are more similar in the subtropical region, resulting in a similar mean between the two algorithms.

Since the NESDIS-processed radiance dataset provides a 15+ year climatology of archived spectral parameters, it is worthwhile investigating the extent to which channels sensitive to the lower troposphere may be corrected to remove the impact of the low cloud cover. As noted above, cloud contamination generally results in a "tail" of cold radiances that introduces a systematic bias in the monthly mean. In these situations, a more robust statistic of the typical clear-sky radiance for a given month may be provided by the mode of the daily measurements for a particular grid box, rather than the mean. By choosing the peak of the frequency distribution, the impact of the outlying (e.g., cloud contaminated) data points upon the estimate of the central tendency is removed. Figure 10 shows a comparison between several zonally averaged 8.2-μm clear-sky quantities: CHAPS monthly mean BT (thick line), NESDIS monthly mean BT (thin line), and NESDIS mode (dotted line). The use of the mode clearly results in improved agreement over the midlat-

itudes, although the agreement is still not perfect. This suggests that the mode, rather than the mean, provides the better estimate of the central tendency of the NESDIS clear-sky 8.2-μm radiance distribution, particularly for regions with extensive low-level cloud cover.

4. Analysis of CHAPS

Satellite-based measurements have improved our understanding of the processes involving global climate change. One example is the use of broadband data from the Earth Radiation Budget Experiment (ERBE) to study the atmospheric greenhouse effect and its relationship to sea surface temperature. Water vapor is the most important gas in the atmospheric feedback mechanism known as the greenhouse effect. Water vapor feedbacks are also a major source of uncertainty in the prediction of climate change. The presence of water vapor affects the radiative properties of the atmosphere and impacts the development of clouds. Observational studies of the radiative effects of water vapor have recently made use of the broadband greenhouse parameters:

$$g = \frac{\sigma T_s^4 - OLR_{cs}}{\sigma T_s^4} \qquad (4)$$

$$G = \frac{\sigma T_s^4}{OLR_{cs}}, \qquad (5)$$

where T_s is the sea surface temperature (SST), σ is the Stefan–Boltzman constant, and OLR_{cs} is the measured clear-sky broadband outgoing longwave flux at the top of atmosphere. The normalized greenhouse parameter [Eq. (4)] was defined by Raval and Ramanathan (1989). Plotted versus SST, the greenhouse parameter is a demonstration of the atmospheric water vapor feedback to SST variation. In addition to providing physical insight into the coupling between the atmosphere and oceans, this parameter is also used to validate climate

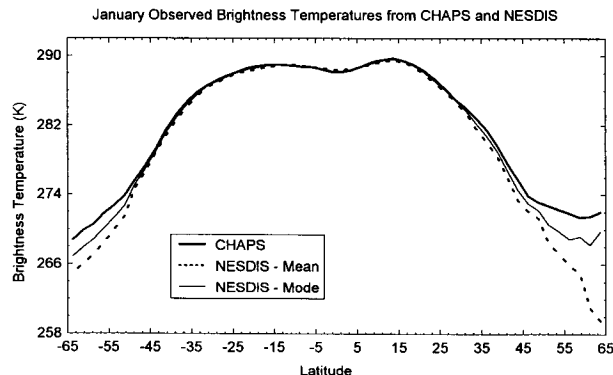January Observed Brightness Temperatures from CHAPS and NESDIS

FIG. 10. Oceanic clear-sky brightness temperature. The thick and thin lines correspond to the zonal mean CHAPS January 1994 data and NESDIS 1981–1990 January data, respectively. The dotted line represents zonal means of NESDIS gridbox mode values.

models. Raval and Ramanathan (1989) illustrated the broadband relationship between the greenhouse parameter and SST and demonstrated that the relationship was mainly due to changes in total column precipitable water content. In addition to understanding the general trend of increasing g with increasing SST, it is important to understand the range in g for a given SST. Stephens and Greenwald (1991) found a similar relationship between g and SST and used simple model calculations to demonstrate that the variability of G [Eq. (5)] as a function of SST was associated with changes in the vertical distribution of water vapor and the temperature lapse rate. Ackerman et al. (1992) used observations to demonstrate the dependency of the greenhouse parameter on upper-tropospheric water vapor using collocated broadband and 6.7-μm spectral observations. They also defined a greenhouse parameter in terms of spectral observations. Webb et al. (1993) used broadband observations and model simulations to explain some of the variability of the relationship between the greenhouse parameter and SST. Understanding the causes of variability in the relationship between the greenhouse parameter and SST is necessary for providing insights into climate variations. The following paragraphs address this issue using clear-sky spectral observations.

The relationship between the spectral greenhouse parameter for wavelengths of 11, 8.2, 7.3, and 6.7 μm and SST are depicted in Figs. 11 and 12 for July 1993 and January 1994, respectively. The quantities shown were generated by averaging over 2.5 degree ERBE grid boxes (ERBE Data Management Team

1991). The higher in the atmosphere that a spectral channel's weighting function peaks (see Table 1), the colder the temperature and therefore the larger the spectral greenhouse parameter. The increase in $g_{8.2}$ and g_{11} with SST is related to the increase in precipitable water with SST. This is similar to the relationship presented by Ackerman et al. (1992) in their regional study using collocated AVHRR, HIRS/2, and ERBE measurements. The coupling of $g_{7.3}$ and $g_{6.7}$ with SST results from large-scale circulation patterns, which are also linked to the SST. The dependence of $g_{8.2}$ and $g_{6.7}$ on SST is demonstrated in Fig. 13, which depicts the brightness temperature of 8.2 and 6.7 μm (BT$_{8.2}$ and BT$_{6.7}$) as a function of SST for the month of January. The dependence of BT$_{11}$ is similar to BT$_{8.2}$, while BT$_{7.3}$ is similar to the dependency of BT$_{6.7}$. The strong dependence on SST in these lower tropospheric-sensitive channels is due, in part, to surface-emitted radiance being transmitted through the atmosphere. Note the change in slope between BT$_{8.2}$ and SST that occurs at an SST of approximately 297 K as noted by Ackerman et al. (1992). The connection between the BT$_{6.7}$ and SST is influenced by atmospheric circulation patterns, which are themselves a function of SST. For example, tropical convection transports moisture into the upper troposphere and is associated with warm SSTs, whereas subsidence dries the upper troposphere and is observed over the cool waters associated with persistent stratus regimes. As the SST increases, BT$_{6.7}$ increases slightly until approximately 290 K after which it remains the same with increasing SST.
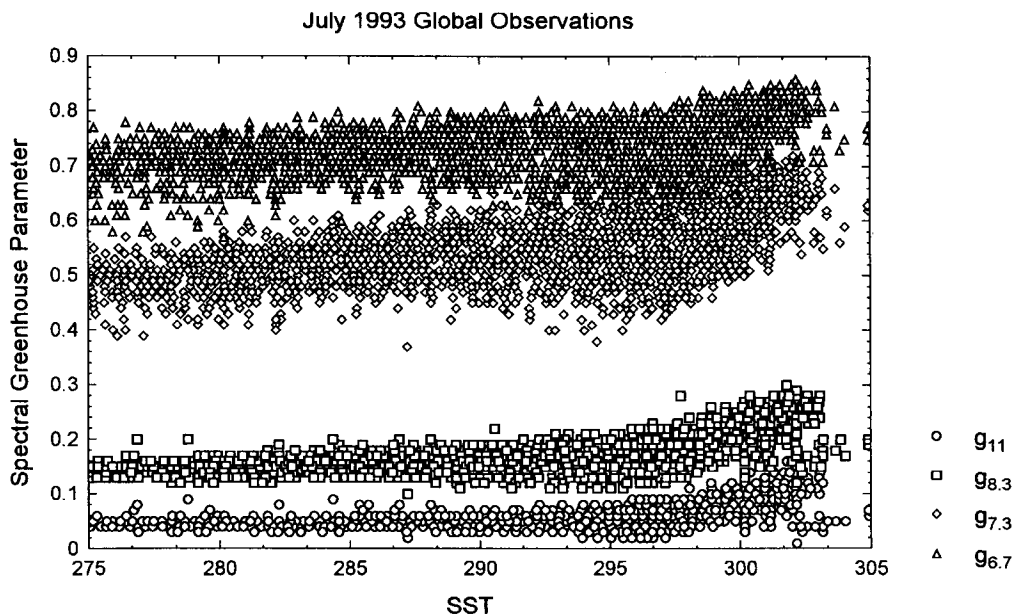

FIG. 11. The spectral greenhouse parameter for wavelengths of 11, 8.2, 7.3, and 6.7 μm as a function of SST for July 1993.

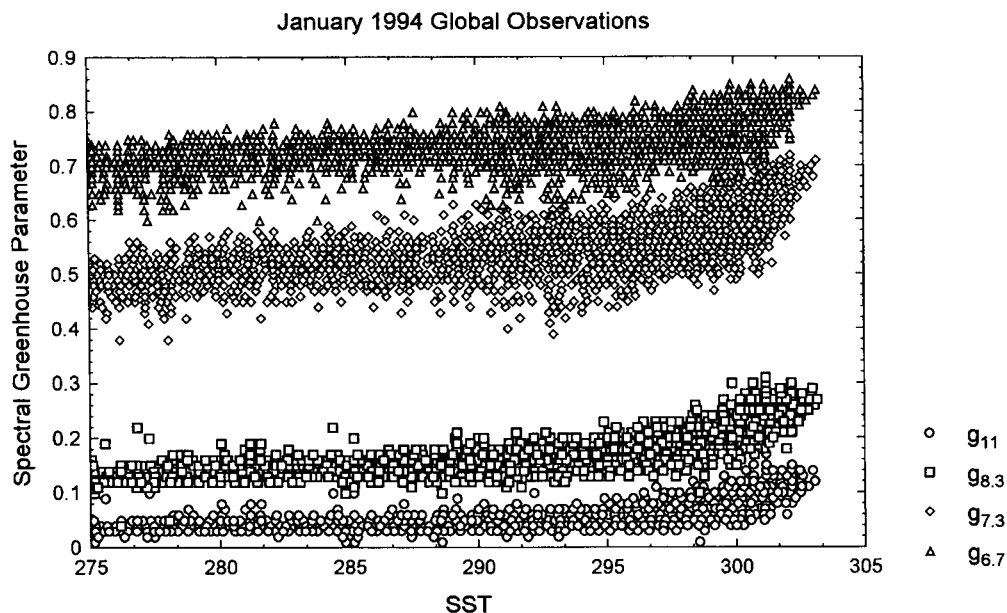## January 1994 Global Observations

FIG. 12. The spectral greenhouse parameter for wavelengths of 11, 8.2, 7.3, and 6.7 μm as a function of SST for January 1994.

As with SST and the broadband greenhouse parameter, g_λ has a geographic dependence. Figures 14a and 14b show the CHAPS monthly mean $g_{6.7}$ and $g_{8.2}$, respectively, for January 1994 (top) and July 1993 (bottom). Dark blue regions are areas where CHAPS did not retrieve high-confidence clear-sky radiances and therefore no greenhouse parameter. From the definition of g_λ, values close to 1 result when the radiant exitance

out the top of the atmosphere has a much smaller magnitude than the radiance entering the bottom of the atmosphere. Spectral regions where the atmosphere is weakly absorbing generally have small values of g_λ. Geographic regions of persistent convection generally have moist atmospheres and, therefore, this is where the spectral greenhouse parameter reaches its maximum value. Regions of persistent subsidence generally
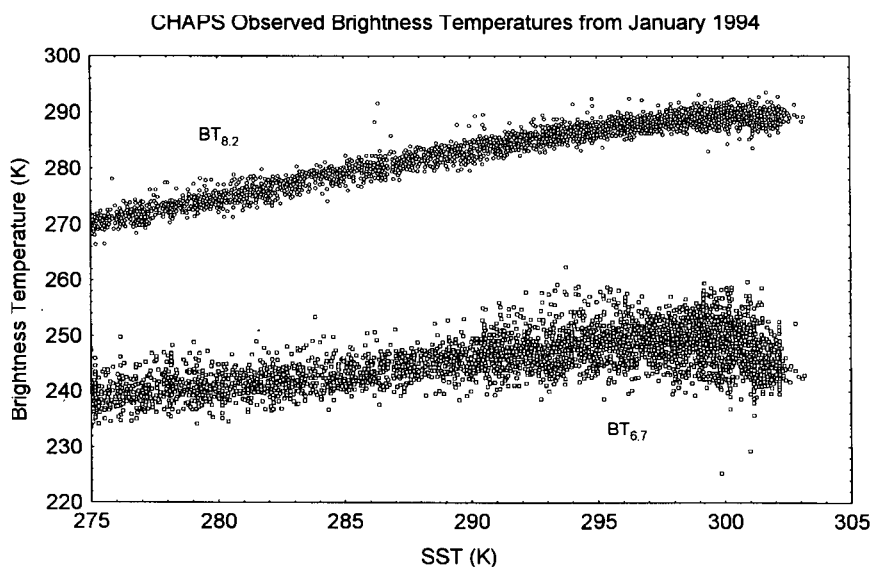
CHAPS Observed Brightness Temperatures from January 1994

FIG. 13. Brightness temperature of 8.2 and 6.7 μm (BT$_{8.2}$ and BT$_{6.7}$) as a function of SST for the month of January.

CHAPS Monthly Mean
6.7 micron spectral greenhouse parameter

January 1994

July 1993

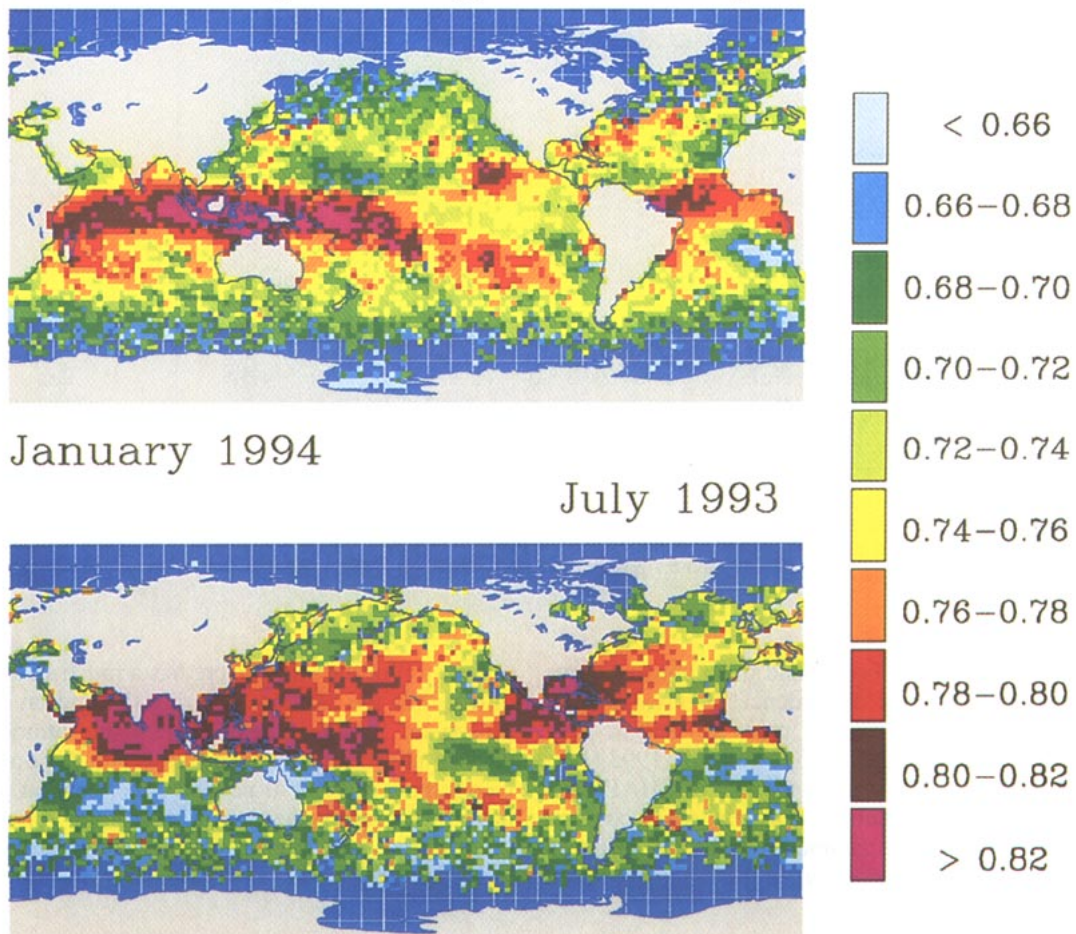|	
	< 0.66
	0.66−0.68
	0.68−0.70
	0.70−0.72
	0.72−0.74
	0.74−0.76
	0.76−0.78
	0.78−0.80
	0.80−0.82
	> 0.82

FIG. 14. (a) Geographic distribution of the CHAPS derived January (top) and July (bottom) monthly mean values of $g_{6.7}$. (b) Geographic distribution of the CHAPS derived January (top) and July (bottom) monthly mean values of $g_{8.2}$.

have dry middle and upper troposphere and thus lower values of g_λ. Oceanic tropical convective regions generally coincide with warm SSTs, while subsident regions west of the continents have oceanic upwelling and cooler SSTs that act to enhance the geographic patterns of g_λ. However, not all regions with warm SSTs have high g_λ values. For example, consider the Arabian Sea during July. This entire body of water is warm, yet there is a strong gradient in $g_{8.2}$. The high values in the eastern Arabian Sea (≈ 0.25) are a consequence of the deep moist layer associated with the southwest summer monsoon. But a low-level temperature inversion exists in the western half, confining much of the moisture to the warm boundary layer, which results in a smaller value of $g_{8.2}$ (≈ 0.17).

Webb et al. (1993) noted that the variability in the broadband greenhouse parameter as a function of SST differed between the winter and summer hemispheres.

By combining the broadband observations with model calculations, they found that water vapor was primarily responsible for variations in the G in the Tropics, whereas temperature variations explained much of the variability in the midlatitudes. The spectral observations of g_λ allow for direct observations of these variations.

Figures 15a–d shows diagrams of g_λ as a function of latitude (negative values are Southern Hemisphere) for HIRS/2 channels 8, 10, 11, and 12 (11, 8.2, 7.3, and 6.7 μm, respectively). Values of the spectral greenhouse parameter were averaged over 10° latitude bands. The center points represent the means and the boxes plus and minus a standard deviation. The solid circles represent January values and the open diamonds July measurements. Maximum values occur in the Tropics where SSTs are warmest and water vapor concentrations greatest. Commonalities are strong between the

CHAPS Monthly Mean
8.2 micron spectral greenhouse parameter

January 1994

July 1993

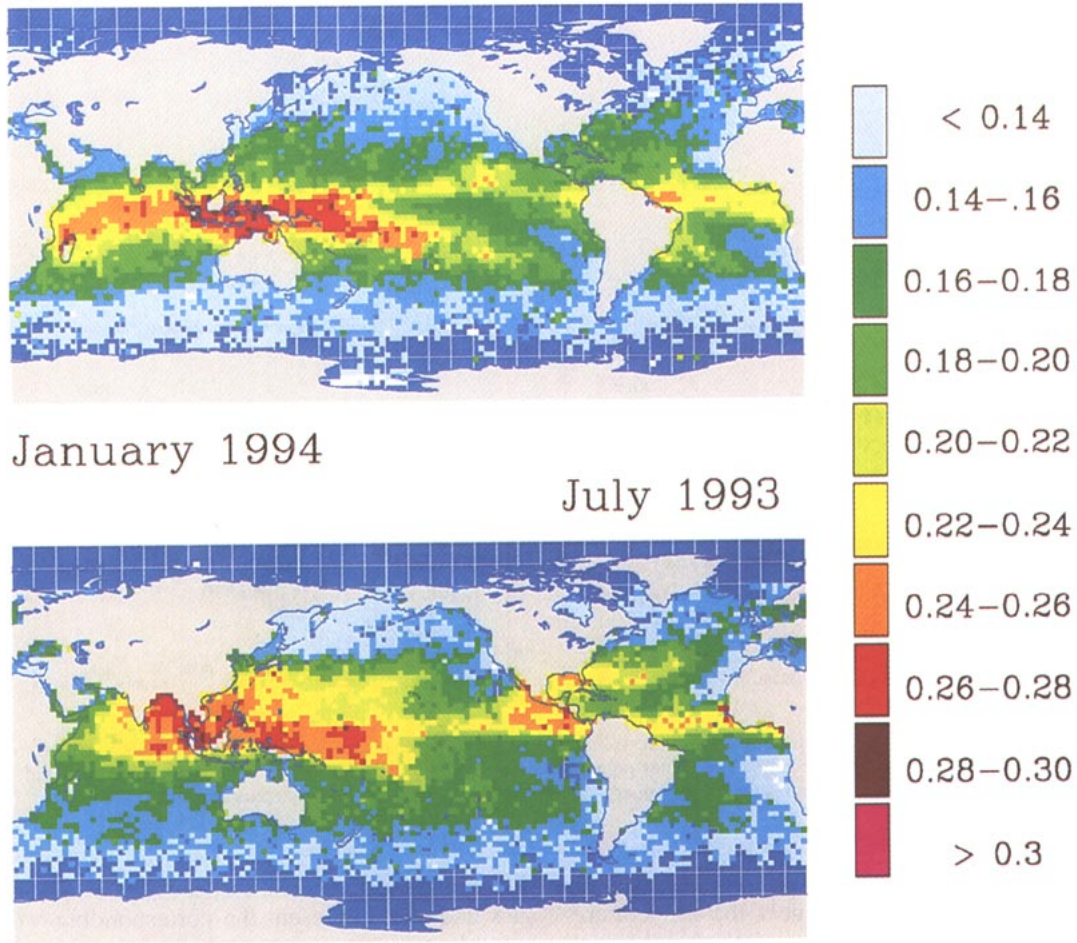|	
	< 0.14
	0.14–.16
	0.16–0.18
	0.18–0.20
	0.20–0.22
	0.22–0.24
	0.24–0.26
	0.26–0.28
	0.28–0.30
	> 0.3

FIG. 14. (Continued)

summer and winter hemispheres. For example, peak values occur within 10 degrees of the equator in the summer hemisphere. For the region between approximately 40°N and 40°S, the latitudinal values of g_λ are seasonally dependent. Except for g_{11}, there is a seasonal symmetry in g_λ—the latitudinal mean value for the Southern Hemisphere summer matches well with the corresponding latitudinal mean value of the Northern Hemisphere summer. The dependence on season is small poleward of 40°. The standard deviations in these plots reveal large variations of g_λ within latitude zones, but which generally decrease toward the poles. This occurs for all four of the HIRS/2 spectral channels sensitive to water vapor. It is also apparent that the standard deviations of g_λ in these water vapor-sensitive bands are somewhat seasonally dependent, especially between 40°N and 40°S. The largest variability across a latitude band occurs in the Tropics and sub-

tropics. This zonal variability decreases with increasing height in the troposphere (as the height of the channels' peak in weighting functions increases). However, there is only small temporal variability during the two months of the study in tropical convective regions (figure not shown).

In addition to the water vapor vertical distribution, the greenhouse effect of the atmosphere is also a function of its temperature structure. Spectral radiance measurements can be used to asses the relative importance of the atmospheric water vapor and temperature distribution in defining the greenhouse parameter. For example, the 14.2-μm radiance (HIRS/2 channel 4) is in a CO_2-absorption band and is primarily sensitive to atmospheric temperature with a peak in the weighting function at approximately 250 mb. Latitudinal variations in the July and January spectral greenhouse parameter at 14.2 μm are depicted in Fig. 16. The $g_{14.2}$ is
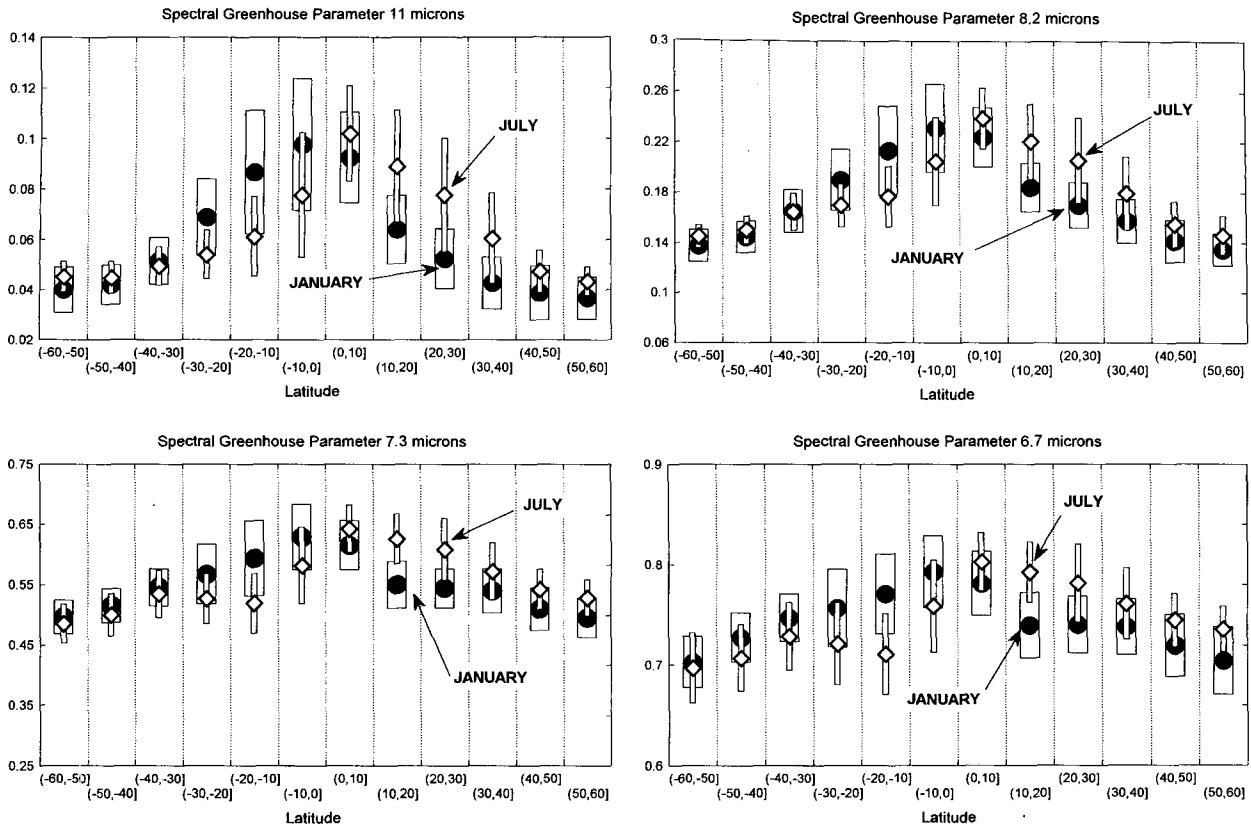
Spectral Greenhouse Parameter 11 microns

Spectral Greenhouse Parameter 8.2 microns

Spectral Greenhouse Parameter 7.3 microns

Spectral Greenhouse Parameter 6.7 microns

FIG. 15. Diagram of g_λ as a function of latitude (negative values are Southern Hemisphere) for HIRS/2 (a) channel 8, (b) 10, (c) 11, and (d) 12 (11, 8.2, 7.3, and 6.7 μm, respectively). The center points represent the latitudinal mean and the boxes denote plus and minus the standard standard deviation. The solid circles represent January values and the open diamonds July measurements.

a strong function of season poleward of approximately 40°. Unlike the water vapor channels, the temperature-sensitive channel shows greatest variation in the mid-latitudes and only small variability in the Tropics.

The seasonal dependence of $g_{14.2}$ and $g_{13.6}$ (HIRS/2 channels 4 and 6) on SST is demonstrated in Fig. 17. The circles and crosses represent $g_{14.2}$ in the summer

and winter hemispheres, respectively, while the triangles and stars represent the corresponding values for $g_{13.6}$. In tropical regions, which are associated with warm oceans, for a given SST, there is a small range of the spectral greenhouse parameter and there is no
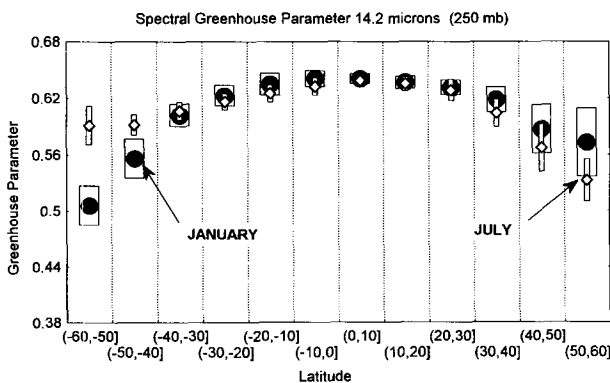
Spectral Greenhouse Parameter 14.2 microns (250 mb)

FIG. 16. Latitudinal variations in the July and January spectral greenhouse parameter at 14.2 μm (see Fig. 15).

Seasonal Dependence of Spectral Greenhouse Parameter
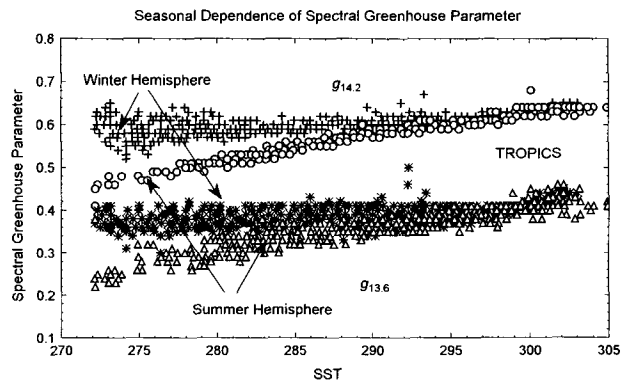

FIG. 17. Spectral greenhouse parameter as a function of SST. The circles and crosses represent the values of $g_{14.2}$ in the summer and winter hemispheres, respectively, while the triangles and stars represent the corresponding values of $g_{13.6}$.

seasonal dependence. In the midlatitude summer hemisphere, as the SST increases, the $g_{14.2}$ and $g_{13.6}$ also increase, which is indicative of a warmer upper troposphere with little variability. During winter, for a given SST colder than approximately 285 K, there is an increased variability in $g_{13.6}$ and $g_{14.2}$. This winter variation is associated with the presence of midlatitude cyclones and accompanying changes in the height of the tropopause as well as changes in the atmospheric lapse rate. The winter troposphere is colder than the summer, which enhances the difference between the effective temperatures of the atmosphere and oceans and leads to a larger $g_{14.2}$ and $g_{13.6}$. The difference in mean lapse rate between winter and summer, 6.03 K km^{-1} versus 5.91 K km^{-1} (Houghton 1986), also contributes to larger values of $g_{14.2}$ and $g_{13.6}$ during winter. In the Tropics, there is little seasonal variation in the tropospheric temperature, and thus smaller variations in $g_{13.6}$ and $g_{14.2}$.

5. Relation between spectral and broadband greenhouse parameters

In this section, we investigate the relationship between the broadband greenhouse parameter g, as measured by ERBE, and the spectral greenhouse parameter g_λ, determined from the NESDIS archived dataset. We have chosen the NESDIS dataset because the CHAPS data do not overlap in time with the ERBE scanner observations. The relationship between the broadband greenhouse parameter and SST has been discussed in several papers (e.g., Raval and Ramanathan 1989; Stephens and Greenwald 1991; Webb et al. 1993). In Figs. 18a and 18b, the abscissa is sea surface temperature and the ordinate is the broadband greenhouse parameter. The shaded regions are an indication of the range of g for a given SST. Corresponding averaged spectral greenhouse parameter values were determined over 1° intervals of SST and over 0.01 in the broadband greenhouse parameter. The shaded areas and contours in Fig. 18a (18b) represent the averaged values of $g_{6.7}$ ($g_{14.0}$) for the given interval of SST and g. This binning is similar to that of Raval et al. (1994), who investigated the dependence of outgoing longwave radiation on sea surface temperature and moisture. Figure 18a demonstrates that for warm SSTs, the range in g is associated with differences in $g_{6.7}$, while for cooler SSTs, variations in $g_{6.7}$ are small and do not explain the large range of g for a given SST. As an example, for an SST of 300 K the broadband greenhouse parameter, g, ranges between approximately 0.33 and 0.4. The smaller values of g are associated with small values of $g_{6.7}$ (0.68) and as g increases to 0.4, $g_{6.7}$ increases to 0.82. For a SST of 280 K, $g_{6.7}$ ranges from 0.7 to 0.72, whereas its broadband counterpart varies from .25 to .35. The ranges of g as a function of a given SST can also be interpreted as occurring due to changes in upper-tropospheric humidity (UTH). Figure 19 is similar to Fig.
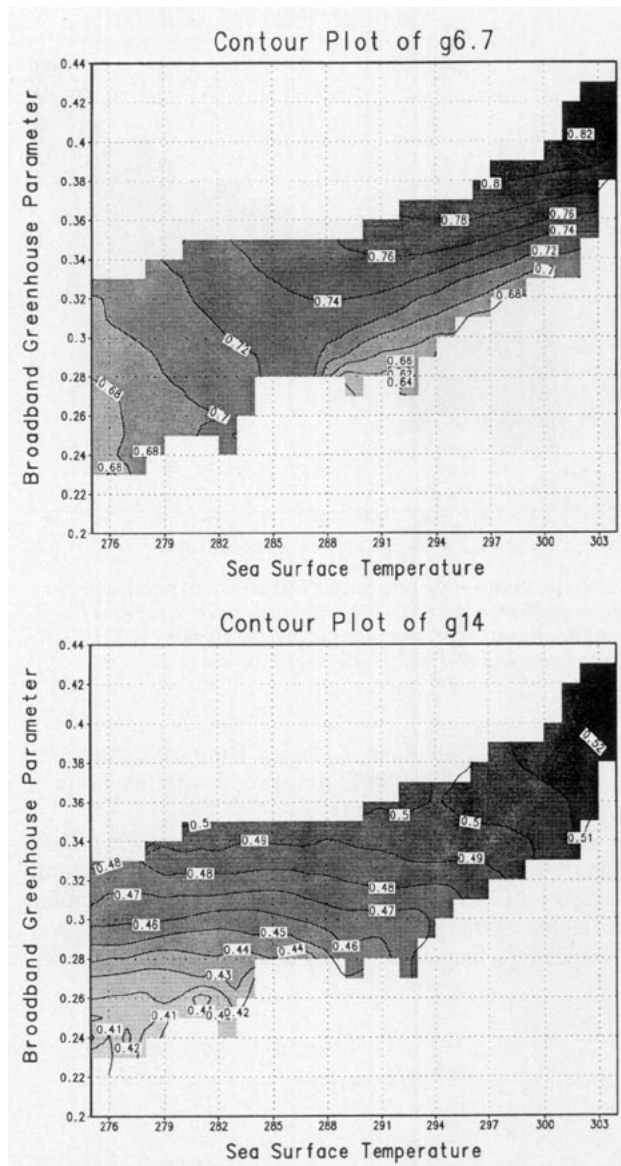

FIG. 18. Relationship between the ERBE-derived broadband greenhouse parameter and SST. The contoured regions represent the averaged values of (a) $g_{6.7}$ and (b) $g_{14.0}$ for the given interval of SST and g. See text for details.

18a, except the contours represent the UTH computed from the HIRS/2 observed 6.7-μm radiances, following the method of Soden and Bretherton (1993). For warm SSTs, the range in g is associated with the magnitude of the UTH. For a given SST, a moist upper troposphere will have a larger g than an atmosphere with a lower UTH. For SSTs less than approximately 288 K, the UTH is relatively uniform, and therefore cannot explain the observed range in g for a given SST.

For cool SSTs, the range in the broadband g is associated with variations in the channels sensitive to upper-tropospheric temperature. Figure 18b shows that
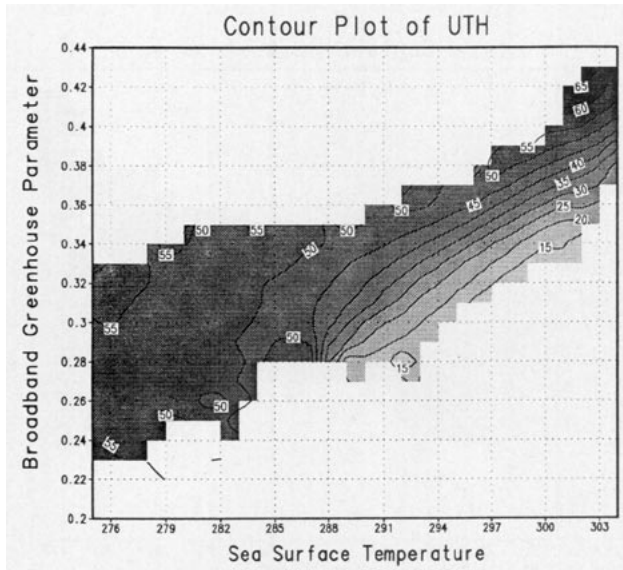
FIG. 19. Relationship between the ERBE derived broadband greenhouse parameter and SST. The contoured region represents the averaged values of upper-tropospheric relative humidity (UTH) for the given interval of SST and g. See text for details.

for a SST of 280 K, $g_{14.0}$ ranges from approximately 0.4 to 0.5. For warm SSTs associated with the Tropics, $g_{14.0}$ shows little variation.

The magnitude of the greenhouse parameter is a function of the total water vapor loading and the temperature structure of the atmosphere. Figures 18 and 19 demonstrate that the range in g for warm, tropical SSTs is driven by spectral changes at wavelengths sensitive to upper-

tropospheric water vapor. For the cooler SSTs, generally associated with the middle latitudes, the range in g is a function of spectral greenhouse parameter sensitive to the temperature structure of the upper troposphere.

The spectral and broadband observations discussed above provide a useful diagnostic tool with which to study relationships between various atmospheric processes that may be associated with climate change. In addition, they provide a reference dataset to use when evaluating the performance of models that predict atmospheric circulations. Understanding model deficiencies through comparisons of model output with observations is not straightforward. For example, it is simple to compare the observed outgoing longwave radiation with model simulations; however, if discrepencies exist, it is sometimes difficult to assess the cause. When agreement occurs, it may not be for the correct reasons, as individual model errors may compensate one another. Including the spectral observations with the broadband measurements provides additional consistency checks. For example, in Fig. 20 the observed broadband and spectral radiative budget parameters are compared with those predicted by the Geophysical Fluid Dynamics Laboratory (GFDL) general circulation model (GCM). The GFDL GCM, described by Wetherald et al. (1991), is a spectral-transform model with 14 vertical levels and is rhomboidally truncated at wavenumber 30, which is approximately equivalent to a horizontal resolution of 2.25° lat × 3.75° long. The model integration was performed for 10 yr (1979–1988) using external conditions prescribed by the Atmospheric Model Intercomparison Project (AMIP). The predicted spectral radiance fields are computed by
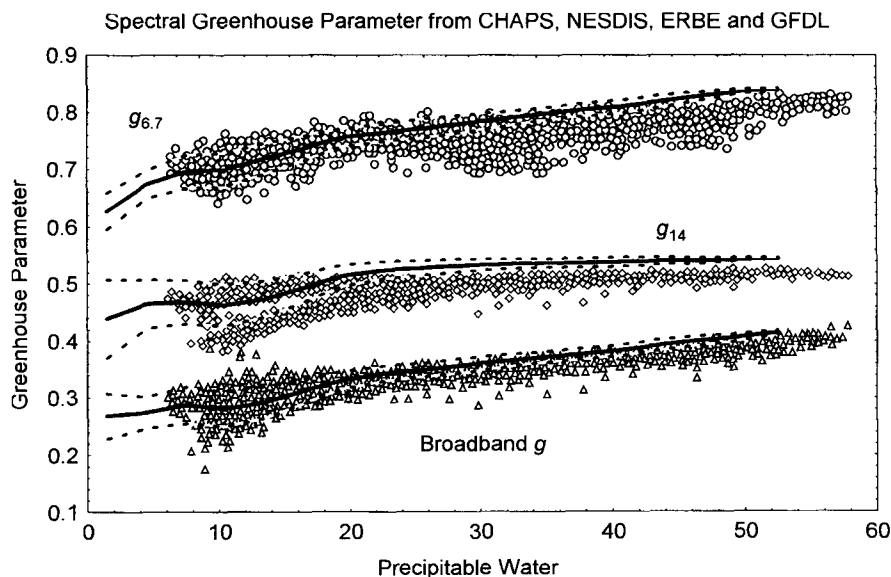

FIG. 20. Relationship between greenhouse parameter and precipitable water. Solid lines represent model output with dashed lines indicating variability. Circles and diamonds are derived NESDIS spectral greenhouse parameter values for $g_{6.7}$ and $g_{14.0}$. Triangles represent ERBE broadband g.

inserting the model profiles of temperature and moisture into the CIMSS transmittance model to simulate the radiance that would be observed by the satellite under those conditions. Both the observed and model results presented here correspond to 4-yr averages from the period 1985–1988. The solid lines represent the mean relationship between the GCM greenhouse parameter and precipitable water (PW), whereas the dashed lines represent the variability as measured by the standard deviation. The points represent observations; the precipitable water was determined from the SSM/I (Special Sensor Microwave Imager) instrument (Liu et al. 1992), the NESDIS spectral (diamonds and circles) and ERBE (triangles) broadband greenhouse parameters were determined as discussed above. For small PW values (less than approximately 20 kg m^{-2}), the model is in agreement with the observations of g, both in magnitude and range. For values of PW greater than approximately 20 kg m^{-2}, the model is overestimating the broadband g and $\Delta g / \Delta PW$. When comparing to the spectral measurements, we see that the model is overestimating both $g_{14.2}$ and $g_{6.7}$ for large PW. The model is also overestimating $\Delta g_{6.7} / \Delta PW$. The observations also exhibit a larger range in $g_{6.7}$ for a given PW than displayed by the model.

6. Summary

Only a few procedures currently exist that derive atmospheric properties using global satellite radiance measurements. ISCCP (e.g., Rossow and Schiffer 1991; Schiffer and Rossow 1983) uses visible and infrared imager data from geostationary and polar-orbiting satellites to derive various cloud products. Wylie et al. (1994) use sounder data to produce global analyses of effective cloud amount and cloud-top pressure. Stowe et al. (1991) use the AVHRR data to develop global cloud products, whereas Rao et al. (1989) present the method used by NOAA to produce global aerosol amount. NESDIS has for many years produced atmospheric temperature and moisture profiles operationally using the TIROS-N Operational Vertical Sounder (e.g., Smith et al. 1979). Many other satellite techniques have been developed for regional applications as well as for deriving global surface properties.

The approach presented in this paper is to collocate observations from the Advanced Very High Resolution Radiometer (AVHRR) and High-resolution Infrared Sounder (HIRS/2) in order to determine global climate parameters. The Collocated HIRS/2 and AVHRR Products (CHAPS) include cloud type and amount, spectral cloud forcing, and the spectral greenhouse parameter, as well as the collocated radiance data. All are available from the authors. The algorithm was run in an operational mode during the months of July 1993, January 1994, and July 1994, though the current study does not present results for July 1994. The authors discuss the CHAPS oceanic clear-sky determination procedure and some analyses of the spectral greenhouse parameter as a function of sea surface temperature, geographic region, and season. The results of the current study can be summarized as follows:

• The capability to collocate imager and sounder data and derive a variety of global climate products in near real time has been demonstrated. Such an approach can easily be adapted to an operational procedure or applied to historical datasets.

• A comparison of CHAPS results with the historical NESDIS clear-sky radiances suggests that the NESDIS 8.2-μm radiances contain a systematic cold bias, particularly over cold, midlatitude oceans. For these regions, the mode rather than the mean, provides a better estimate of the central tendency of the NESDIS clear-sky 8.2-μm radiance distribution.

• The spectral greenhouse parameter measured in water vapor-sensitive channels with weighting functions peaking in the lower atmosphere have values that are directly coupled to the SST. In channels sensitive to middle and upper-tropospheric water vapor, g_λ is also dependent on SST via its connection to large-scale atmospheric circulation patterns. The spectral greenhouse parameter measured in all the water vapor–sensitive channels are dependent on the atmospheric total precipitable water, increasing with increasing water vapor loading.

• Water vapor–sensitive channels display latitudinal variations of the spectral greenhouse parameter, which generally decrease poleward, in agreement with the simulations of Webb et al. (1993). These channels show large standard deviations of g_λ with latitude.

• The water-vapor-sensitive channels display the largest variability of g_λ in the Tropics, whereas $g_{14.2}$ has minimum variability in the Tropics and largest variation in the midlatitudes. These spectral observations support the broadband study of Webb et al. (1993).

• Variability in the relationship between g_λ sensitive to water vapor and SST shows only a weak dependence on season. A strong seasonal dependence is observed, however, for the 14.2-μm upper-tropospheric temperature-sensitive channel. Large variations are observed in the winter hemisphere and are likely associated with changes in the height of the tropopause and in the vertical temperature structure of the atmosphere during the progression of midlatitude cyclones.

• For warm SSTs, the range in the broadband greenhouse parameter, g, is associated with changes in the spectral greenhouse parameter sensitive to upper-tropospheric water vapor. For cooler SSTs, the range in the broadband g is associated with changes in the spectral greenhouse parameter sensitive to upper-tropospheric temperature.

REFERENCES

Ackerman, S. A., R. A. Frey, and W. L. Smith, 1992: Radiation budget studies using collocated observations from AVHRR, HIRS/2, and ERBE instruments. *J. Geophys. Res.*, **97**, 11 513–11 525.

Aoki, T., 1980: A method for matching the HIRS-2 and AVHRR pictures of *TIROS-N* satellites. Meteorological Satellite Center Tech. Note 2, Tokyo, Japan, 15–26.

Bates, J. J., and X. Wu, 1995: Interannual variability of upper troposphere water vapor band brightness temperature. *J. Climate*, submitted.

Baum, R. A., B. A. Wielicki, and P. Minnis, 1992: Cloud-property retrieval using merged HIRS and AVHRR data. *J. Appl. Meteor.*, **31**, 351–369.

——, R. F. Arduini, B. A. Wielicki, P. Minnis, and S.-C. Tsay, 1994: Multilevel cloud retrieval using multispectral HIRS and AVHRR Data: Nighttime oceanic analysis. *J. Geophys. Res.*, **99**, 5499–5514.

Brown, S. R., 1991: Amendments to NOAA Tech. Memo., NESS 107, Appendix B, Memorandum, 1 pp.

Derrien, M., B. Farki, L. Harang, H. LeGleau, A. Noyalet, D. Pochic, and A. Sairouni, 1993: Automatic cloud detection applied to NOAA-11/AVHRR imagery. *Remote Sens. Environ.*, **46**, 246–267.

ERBE Data Management Team, 1991: Earth radiation budget experiment (ERBE) data management system: The regional, zonal, and global gridded averages: S-4G user's guide. Report ERBE 3-3-12-11-91-01-0, NASA Langley Research Center, Hampton, VA, 103 pp.

Hayden, C. M., and B. F. Taylor, 1985: The application of AVHRR data to fine scale temperature and moisture retrievals obtained from NOAA satellites. Preprints, *14th Conf. on Severe Local Storms*, Indianapolis, IN, Amer. Meteor. Soc., J22–J28.

Houghton, J. T., 1986: *The Physics of Atmospheres.* Cambridge University Press, 271 pp.

Inoue, T., 1987: A cloud type classification with *NOAA 7* split window measurements. *J. Geophys. Res.*, **92**, 3991–4000.

Kidwell, K. B., 1991: NOAA Polar Orbiter Users Guide. U.S. Dept. Commerce, 377 pp.

Levanant, L., 1989: AVHRR/HIRS coupling. *Proc. Fifth Int. TOVS Conf.*, Toulouse, France, LMD, 247–259.

Liu, T. T., W. Tang, and F. Wentz, 1992: Precipitable water and surface humidity over oceans for the SSM/I and ECMWF. *J. Geophys. Res.*, **97**, 2251–2264.

Menzel, W. P., W. L. Smith, and T. R. Stewart, 1983: Improved cloud motion wind vector and altitude assignment using VAS. *J. Appl. Meteor.*, **22**, 377–384.

McClain, E. P., 1989: Global sea surface temperatures and cloud clearing for aerosol optical depth estimates. *Int. J. Remote Sens.*, **10**, 763–769.

McMillin, L. M., and C. Dean, 1982: Evaluation of a new operational technique producing clear radiances. *J. Appl. Meteor.*, **21**, 1005–1014.

Rao, C. R. N., L. L. Stowe, and E. P. McClain, 1989: Remote sensing of aerosols over the oceans using AVHRR data: Theory, practice and application. *Int. J. Remote Sens.*, **10**, 743–749.

Raval, A., A. H. Oort, and V. Ramaswamy, 1994: Observed dependence of outgoing longwave radiation on sea surface temperature and moisture. *J. Climate*, **7**, 807–821.

Raval, R., and V. Ramanathan, 1989: Observation determination of the greenhouse effect. *Nature*, **342**, 758–761.

Rossow, W. B., and R. A. Schiffer, 1991: ISCCP cloud data products. *Bull. Amer. Meteor. Soc.*, **72**, 2–20.

Schiffer, R. A., and W. B. Rossow, 1983: The International Satellite Cloud Climatology Project (ISCCP): The first project of the World Climate Research Programme. *Bull. Amer. Meteor. Soc.*, **64**, 779–784.

Smith, W. L., and C. M. R. Platt, 1978: Comparison of satellite-deduced cloud heights with indications from radiosonde and ground-based laser measurements. *J. Appl. Meteor.*, **17**, 1796–1802.

——, H. M. Woolf, P. G. Abel, C. M. Hayden, M. Chalfant, and N. Grody, 1974: Nimbus 5 sounder data processing system. Part 1: Measurement characteristics and data reduction procedures. NOAA Tech. Memo., NESS 57, Washington, DC, 99 pp.

——, ——, C. M. Hayden, D. Q. Wark, and L. M. McMillin, 1979: The *TIROS-N* operational vertical sounder. *Bull. Amer. Meteor. Soc.*, **60**, 1127–1150.

Soden, B. J., and F. P. Bretherton, 1993: Upper tropospheric relative humidity from the GOES 6.7 micron channel: Method and climatology for July 1987. *J. Geophys. Res.*, **98**, 16 669–16 688.

Stephens, G. L., 1990: On the relationship between water vapor over the oceans and sea surface temperature, *J. Climate*, **3**, 634–645.

——, and T. J. Greenwald, 1991: The earth's radiation budget and its relation to atmospheric hydrology. Part 1: Observations of the clear-sky greenhouse effect. *J. Geophys. Res.*, **96**, 15 325–15 340.

Stowe, L. L., E. P. McClain, R. Carey, P. Pellegrino, G. Gutman, P. Davis, C. Long, and S. Hart, 1991: Global distribution of cloud cover derived from NOAA/AVHRR operational satellite data. *Adv. Space Res.*, **11**, 51–54.

Strabala, K. I., S. A. Ackerman, and W. P. Menzel, 1994: Cloud properties inferred from 8-12-μm data. *J. Appl. Meteor.*, **33**, 212–229.

Suomi, V. E., R. J. Fox, S. S. Limaye, and W. L. Smith, 1983: McIDAS III, a modern interactive data analysis facility. *J. Appl. Meteor.*, **22**, 766–788.

Webb, M. J., A. Slingo, and G. L. Stephens, 1993: Seasonal variation of the clear-sky greenhouse effect: The role of changes in atmospheric temperatures and humidities. *Climate Dyn.*, **9**, 117–129.

Wetherald, R. T., V. Ramaswamy, and S. Manabe, 1991: A comparative study of the observations of high clouds and simulations by an atmospheric general circulation model. *Climate Dyn.*, **5**, 135–143.

Wylie, D. P., W. P. Menzel, H. M. Woolf, and K. I. Strabala, 1994: Four years of global cirrus cloud statistics using HIRS. *J. Climate*, **7**, 1972–1986.